

Orientation preferences of extended sub-granular dislocation boundaries

Sivasambu Mahesh ^{a,*}

^aDepartments of Mechanical and Aerospace Engineering,
 Indian Institute of Technology, Kanpur 208016. India.

(Received 00 Month 200x; final version received 00 Month 200x)

The orientation and disorientation of extended cell block boundaries that separate cell blocks in model rate-independent grains accommodating imposed plastic deformation by the mechanism of slip is predicted on the basis of the following three hypotheses: (1) a uniform state of stress prevails throughout the grain, (2) cell blocks are disoriented so as to minimize the power of plastic deformation and (3) cell block boundaries are oriented so as to minimize plastic incompatibility between neighboring cell blocks. Predicted orientations and disorientations compare favorably with those reported in the experimental literature for copper and aluminum polycrystals deformed plastically in uniaxial tension. This suggests that the assumed hypotheses may represent the physical principles that determine the preferred cell block boundary orientation.

Keywords: dislocation structures; microstructure; micromechanics; numerical simulation

1. Introduction

Texture and plastic anisotropy of grains together introduce anisotropy in the plastic response of polycrystals [1–5]. Anisotropy at the grain level arises due to oriented sub-structural features [6] called cell block boundaries (CBBs). CBBs are geometrically necessary dislocation boundaries [7] that accommodate incompatibility in the plastic deformation field. In medium to high stacking fault energy metals, like copper and aluminum, approximately parallel CBBs are observed to separate regions called cell blocks (CBs) only a few microns thick but several tens of microns long [6]. CBBs render the plastic response of the grain anisotropic because greater resolved shear stress is required to activate slip in systems that intersect CBBs than in systems that are aligned parallel to CBBs. Existing sub-structure based hardening models [3–5, 8, 9] can already account for such mechanical anisotropy provided the correct CBB orientation is supplied to them. Predicting the crystallographic orientation of CBBs is therefore an important step toward developing improved physically based models of single crystal and polycrystal plasticity.

The orientation of CBBs relative to the crystallographic slip planes has been the subject of extensive experimental investigation [6, 10–21]. These investigations have focused on tensile or rolling deformation of medium to high stacking fault metal and alloy polycrystals. Under tensile deformation, there is widespread agreement amongst the experimental studies [11, 13, 19–21] that a systematic classification of grains into three types occurs: Type 1 grains, which show close coincidence of one set of parallel CBBs with a crystallographic slip plane, Type 2 grains, wherein the CBB structure does not form and Type 3 grains, in which the CBBs do not

*Corresponding author. Tel: +91 512 259 6087. Email: smahesh@iitk.ac.in

align with any crystallographic slip plane. Such a clear correlation between grain orientation and sub-structure has not been found in rolled polycrystals [10, 14, 17]. Instead, CBBs are found to be inclined close to $35^\circ - 40^\circ$ with the rolling direction.

Although a comprehensive theoretical explanation of these experimental observations is not presently available, Winther and co-workers [12, 15, 16, 20, 21] have demonstrated that the distribution of slip activity amongst the slip systems of a grain and the type of dislocation wall structure that develops in it are highly correlated. Winther et al [12] observed that crystallographic CBBs form in grains in which two coplanar slip systems account for most of the slip activity in the grain. They proposed that crystallographic CBBs are constituted of slip dislocations generated from coplanar slip activity. Regardless of whether the CBB is crystallographic or otherwise, Winther et al [15] and Winther [16, 21] have established that CBB orientation is much more influenced by crystallographic, rather than macroscopic influences, in that CBB planes are closely aligned with certain crystallographic planes, while being widely scattered about the planes of maximum shear stress. Winther and Huang [20] have classified slip system activity into slip classes. They have associated specific types of dislocation structures with each slip class. They have also shown that different types of imposed deformation that cause the activation of slip systems within the same slip class result in the creation of the same type of dislocation sub-structure. A different theoretical explanation, due to Wert and Huang [22], holds that CBBs align with equivalent slip planes. This explanation reasonably predicts the observed CBB alignment in four symmetric crystal orientations. It has, however, not been more widely tested.

In uniaxial tension of polycrystals [6, 11, 13, 14], CBB orientation in each grain is observed to depend only on its final lattice orientation. In experiments involving a deformation path change [3–5], the CBB structure formed during the first path is annihilated within a few percent of straining along the second path and replaced with a structure that is consistent with the slip distribution of the latter. **In a copper polycrystal subjected to rolling deformation**, Christoffersen and Leffers [23] observed that CBB orientations do not evolve in accordance with the grain shape evolution; their rotation toward the rolling plane occurs at a smaller rate than that suggested by the grain shape evolution. These observations suggest that the CBB structure in a grain at any instant of deformation is mostly governed by the state of slip activity at that instant and not as much on the history of past deformation [20, 21]. CBBs, at low accumulated strains (von Mises strain ≤ 0.5), thus appear to be unstable dislocation boundaries that are continuously broken up and restored or replenished [24] during deformation. At higher strains, Albou et al. [24] have suggested that the development of immobile pinning points due to secondary slip may result in further evolution of their orientation in conformity with the grain shape.

The present work seeks to explain CBB orientation and disorientation **at low accumulated strains** within the framework of **local** rate-independent crystal plasticity supplemented by three hypotheses pertaining to a grain modeled as a collection of interacting material points, representing CBs. The internal variables of the model are the disorientation angle between adjacent CBs and the hardness of its slip systems. The modeling framework described in Section 2 determines not only the deviatoric stresses and slip rates in the CBs but also the CBB orientation and disorientation axis, **the rate of evolution of geometrically necessary dislocation densities associated with CBBs and CBB misorientation rates** for a given imposed deformation. **Because the present local framework does not account for any intrinsic material length scales, the rate of change of CBB spacing is not predicted presently.** The predictions given in Section 3 compare favorably with experimental

observations reported in the literature.

2. Model

2.1. Rate-independent crystal plasticity

2.1.1. Constitutive law

The constitutive response of every material point in the model grain is assumed to follow standard rate-independent crystal plasticity [25]. Following the Taylor-Bishop-Hill formulation [26, 27], the slip-rate tensor at a material point, \mathbf{L}_{ss} , is given by

$$\mathbf{L}_{ss} = \sum_{s=1}^S \dot{\gamma}_s \mathbf{b}_s \otimes \mathbf{n}_s, \quad (1)$$

where $\dot{\gamma}_s$ denotes the slip rate in slip system $s \in \{1, 2, \dots, S\}$ and where \mathbf{b}_s is the Burger's vector or unit slip directional vector of slip system s with slip plane normal \mathbf{n}_s . The strain-rate at the material point, $\dot{\boldsymbol{\epsilon}}$, is the symmetric part of \mathbf{L}_{ss} :

$$\dot{\boldsymbol{\epsilon}} = \frac{\mathbf{L}_{ss} + \mathbf{L}_{ss}^T}{2} = \sum_{s=1}^S \dot{\gamma}_s \mathbf{m}_s, \quad (2)$$

where, \mathbf{m}_s denotes the Schmid tensor of slip system s :

$$\mathbf{m}_s = (\mathbf{b}_s \otimes \mathbf{n}_s + \mathbf{n}_s \otimes \mathbf{b}_s)/2. \quad (3)$$

Slip rates $\dot{\gamma}_s$ are required to be non-negative: $\dot{\gamma}_s \geq 0$. Positive and negative senses of the slip direction, $\pm \mathbf{b}_s$, are distinguished so that slip systems with Schmid tensors $+\mathbf{m}_s$ and $-\mathbf{m}_s$ are considered distinct. Since $\text{tr } \mathbf{m}_s = \mathbf{b}_s \cdot \mathbf{n}_s = 0$, plastic deformation by the mechanism of slip is volume conserving, i.e.,

$$\text{tr } \dot{\boldsymbol{\epsilon}} = 0. \quad (4)$$

If \mathbf{L} denotes the imposed velocity gradient at the material point, its lattice spin tensor $\dot{\mathbf{W}}$ is given by [25]

$$\dot{\mathbf{W}} = \mathbf{L} - \mathbf{L}_{ss}. \quad (5)$$

The lattice spin tensor is skew-symmetric: $\dot{\mathbf{W}} = -\dot{\mathbf{W}}^T$.

Let $p \in \{1, 2, \dots, P\}$ denote the set of distinct crystallographic slip planes amongst the slip systems. Let \mathbf{N}_p denote the normal to the p -th crystallographic plane. Further, let $\dot{\Gamma}_p$ denote the total slip rate in the p -th crystallographic slip plane,

$$\dot{\Gamma}_p = \sum_{s \in \mathcal{S}} \dot{\gamma}_s, \quad (6)$$

where, \mathcal{S} denotes the set of slip systems associated with the p -th crystallographic slip plane: $\mathbf{N}_p = \pm \mathbf{n}_s$ for $s \in \mathcal{S}$.

Let $\boldsymbol{\sigma}$ denote the deviatoric part of the Cauchy stress at the material point. Schmid's law [25] states that slip system s may have non-zero slip-rate only if the resolved shear stress, $\boldsymbol{\sigma} : \mathbf{m}_s \equiv \text{tr}(\boldsymbol{\sigma} \mathbf{m}_s^T)$, equals the critical resolved shear stress on slip system s , τ_s . Thus,

$$\dot{\gamma}_s \begin{cases} \geq 0, & \text{if } \boldsymbol{\sigma} : \mathbf{m}_s = \tau_s, \\ = 0, & \text{if } \boldsymbol{\sigma} : \mathbf{m}_s < \tau_s. \end{cases} \quad (7)$$

Slip systems are assumed not to harden in the present work:

$$\dot{\tau}_s = 0. \quad (8)$$

Taylor's principle [26] asserts that for given $\dot{\boldsymbol{\epsilon}}$ of all possible slip-rate combinations $\{\dot{\gamma}_s, s \in \{1, \dots, S\}\}$ that obey the constraint given by Equation (2), only those which minimize the plastic power density

$$P = \sum_{s=1}^S \tau_s \dot{\gamma}_s = \boldsymbol{\sigma} : \dot{\boldsymbol{\epsilon}} \quad (9)$$

are valid solutions. The equivalence between the second and third terms was shown by Chin and Mammel [28].

2.2. Idealized geometry of the grain substructure

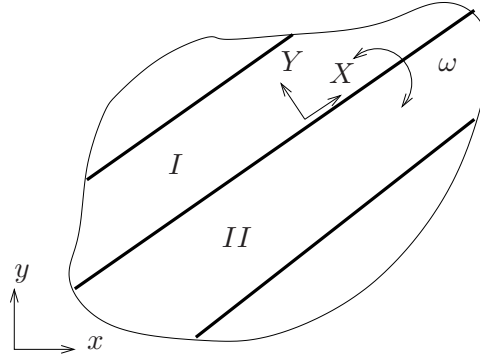


Figure 1. Schematic diagram of a small part of a grain located well away from the grain boundaries showing two cell blocks, I and II .

A pair of neighboring interacting CBs, denoted I and II , which are equal in volume is shown in Figure 1. Each CB is assumed to have a uniform lattice orientation. The CBs are, however, mutually disoriented; the disorientation angle is denoted by ω . In accordance with experimental observations [6, 14], the domain of the entire grain, which is much larger than the section shown in Figure 1, is assumed to be patterned repetitively by CBs of types I and II . The CBB separating two CBs is idealized as a planar infinitesimally thin dislocation wall that may move relative to the material of the CBs. Continuous break-up and restoration of CBBs by stress-assisted dynamic recovery and dislocation migration across CBBs and trapping at CBBs have been proposed as possible mechanisms for the apparent motion of CBBs relative to the material [8, 24].

Velocity gradient $\bar{\mathbf{L}}$, whose symmetric part is denoted $\bar{\boldsymbol{\epsilon}} = (\bar{\mathbf{L}} + \bar{\mathbf{L}}^T)/2$, is externally imposed upon the grain. Each CB is assumed to deform homogeneously

and can therefore be represented by a single material point. The velocity gradients of material points in CB I and CB II will be denoted $\mathbf{L}^{(I)}$ and $\mathbf{L}^{(II)}$, respectively. The corresponding strain-rates are denoted $\dot{\boldsymbol{\epsilon}}^{(I)} = (\mathbf{L}^{(I)} + \mathbf{L}^{(I)T})/2$ and $\dot{\boldsymbol{\epsilon}}^{(II)} = (\mathbf{L}^{(II)} + \mathbf{L}^{(II)T})/2$, respectively. Equations (A2) and (A3) in Appendix A relate the CB velocity gradient and strain-rate to those externally imposed as

$$\begin{aligned}\bar{\mathbf{L}} &= (\mathbf{L}^{(I)} + \mathbf{L}^{(II)})/2 \text{ and} \\ \bar{\boldsymbol{\epsilon}} &= (\dot{\boldsymbol{\epsilon}}^{(I)} + \dot{\boldsymbol{\epsilon}}^{(II)})/2,\end{aligned}\tag{10}$$

where the factor 1/2 is the volume fraction, $\rho^{(i)}$, assumed equal, of each of the two CB types.

2.3. Continuity conditions across CBBs: Hypothesis 1

Hypothesis 1: The deviatoric stress state is uniform across both CB I and CB II :

$$\boldsymbol{\sigma}^{(I)} = \boldsymbol{\sigma}^{(II)} = \bar{\boldsymbol{\sigma}},\tag{11}$$

where $\bar{\boldsymbol{\sigma}}$ represents the uniform deviatoric stress state in both CBBs. Because of the assumption of repetitious patterning of the entire grain by the two CB types (Section 2.2), Hypothesis 1 amounts to assuming a uniform deviatoric stress over the entire grain. Compatible deformation of CBs requires continuity of the velocity field across the intervening CBB [29]. This is not enforced by Hypothesis 1 and leads, in general, to misfit-strains across CBBs, which must be locally accommodated to maintain material continuity across them [7, 30]. In the present model, the plastic power density associated with local accommodation is assumed to be negligible.

The problem of determining the deformation rates of the two CBs according to Hypothesis 1 may be stated as follows: It is required to determine the slip-rates, $\dot{\gamma}_s^{(I)}$ and $\dot{\gamma}_s^{(II)}$, in slip systems $s \in \{1, 2, \dots, S\}$ of the two CBs such that (i) Schmid's law, given by Equation (7),

$$\dot{\gamma}_s^{(I)} \begin{cases} \geq 0, & \text{if } \bar{\boldsymbol{\sigma}} : \mathbf{m}_s^{(I)} = \tau_s, \\ = 0, & \text{if } \bar{\boldsymbol{\sigma}} : \mathbf{m}_s^{(I)} < \tau_s. \end{cases}\tag{12}$$

and

$$\dot{\gamma}_s^{(II)} \begin{cases} \geq 0, & \text{if } \bar{\boldsymbol{\sigma}} : \mathbf{m}_s^{(II)} = \tau_s, \\ = 0, & \text{if } \bar{\boldsymbol{\sigma}} : \mathbf{m}_s^{(II)} < \tau_s \end{cases}\tag{13}$$

holds in each of the CBs and (ii) such that the strain-rates, $\dot{\boldsymbol{\epsilon}}^{(I)}$ and $\dot{\boldsymbol{\epsilon}}^{(II)}$ satisfy Equation (10). $\mathbf{m}_s^{(I)}$ and $\mathbf{m}_s^{(II)}$ denote the Schmid tensors of the s -th slip system in CB I and CB II , respectively. The strain-rates are given by

$$\begin{aligned}\dot{\boldsymbol{\epsilon}}^{(I)} &= \sum_s \dot{\gamma}_s^{(I)} \mathbf{m}_s^{(I)}, \\ \dot{\boldsymbol{\epsilon}}^{(II)} &= \sum_s \dot{\gamma}_s^{(II)} \mathbf{m}_s^{(II)},\end{aligned}\tag{14}$$

according to Equation (2). The plastic power, P_1 , associated with grain deformation that follows Hypothesis 1 is

$$\begin{aligned} P_1 &= \rho^{(I)} \bar{\boldsymbol{\sigma}} : \dot{\boldsymbol{\epsilon}}^{(I)} + \rho^{(II)} \bar{\boldsymbol{\sigma}} : \dot{\boldsymbol{\epsilon}}^{(II)} \\ &= \bar{\boldsymbol{\sigma}} : (\rho^{(I)} \dot{\boldsymbol{\epsilon}}^{(I)} + \rho^{(II)} \dot{\boldsymbol{\epsilon}}^{(II)}) \\ &= \bar{\boldsymbol{\sigma}} : \bar{\dot{\boldsymbol{\epsilon}}}, \end{aligned} \tag{15}$$

using Equation (10). P_1 of Equation (15) is thus the same as P_{\min} in Equation (A8) of Appendix A. By the lower bound theorem, P_1 can therefore be no greater than the plastic power dissipated during the compatible deformation of the two CBs.

2.4. Disorientation axis of CBBs: Hypothesis 2

As stated in Section 2.2 neighboring CBs are assumed to be disoriented by a small angle ω . This disorientation may, for instance, be introduced by statistically trapped incidental dislocation boundaries formed during plastic deformation. The unit disorientation axes $\hat{\boldsymbol{\mu}}$ across incidental dislocation boundaries are known to be uniformly distributed [31].

Hypothesis 2: Of all possible unit disorientation axes, $\hat{\boldsymbol{\mu}}$, distributed over the unit sphere, CBs disorient preferentially about the disorientation axis $\boldsymbol{\mu}$, which minimizes the plastic power density of the grain, P_1 , given by Equation (15) subject to the constraints of Equations (10), (12), (13) and (14).

For fixed disorientation angle ω , the Schmid tensors $\mathbf{m}_s^{(I)}$ and $\mathbf{m}_s^{(II)}$ of the two CBs depend on the disorientation axis, $\hat{\boldsymbol{\mu}}$. For, if $\mathbf{R}(\omega, \hat{\boldsymbol{\mu}})$ denotes the orthonormal tensor that represents a rotation of ω about the axis $\hat{\boldsymbol{\mu}}$, $\{\mathbf{m}_s^{(I)}, \mathbf{m}_s^{(II)} : s \in \{1, 2, \dots, S\}\}$ obey

$$[\mathbf{m}_s^{(I)}] = [\mathbf{R}(\omega, \hat{\boldsymbol{\mu}})][\mathbf{m}_s^{(II)}][\mathbf{R}(\omega, \hat{\boldsymbol{\mu}})]^T. \tag{16}$$

Together with Equations (12) and (13), this implies that the uniform stress tensor, $\bar{\boldsymbol{\sigma}}$ also depends on $\hat{\boldsymbol{\mu}}$ and justifies the notation $\bar{\boldsymbol{\sigma}}(\hat{\boldsymbol{\mu}})$.

The identification of the CBB disorientation $\boldsymbol{\mu}$ in accordance with the two hypotheses given above can be posed in the framework of a two-level optimization problem. The upper-level optimization problem is simply the mathematical expression of Hypothesis 2 above and can be stated as:

$$\boldsymbol{\mu} = \underset{\hat{\boldsymbol{\mu}}}{\operatorname{argmin}} \bar{\boldsymbol{\sigma}}(\hat{\boldsymbol{\mu}}) : \bar{\dot{\boldsymbol{\epsilon}}}. \tag{17}$$

Note that $\underset{\mathbf{x}}{\operatorname{argmin}} f(\mathbf{x})$ denotes the value(s) of \mathbf{x} at which the function $f(\mathbf{x})$ is minimum. The determination of $\bar{\boldsymbol{\sigma}}(\hat{\boldsymbol{\mu}})$ for fixed $\hat{\boldsymbol{\mu}}$ through an extension of the Taylor-Bishop-Hill [26, 27] formulation constitutes the lower-level optimization problem. It follows from the Karush-Kuhn-Tucker theorem [28, 32, 33] that the lower-level problem is solved by the uniform deviatoric stress field $\hat{\boldsymbol{\sigma}}$ that maximizes the external power of plastic deformation, i.e.,

$$\bar{\boldsymbol{\sigma}}(\hat{\boldsymbol{\mu}}) = \underset{\hat{\boldsymbol{\sigma}}}{\operatorname{argmax}} \hat{\boldsymbol{\sigma}}(\hat{\boldsymbol{\mu}}) : \bar{\dot{\boldsymbol{\epsilon}}}, \tag{18}$$

where maximization is subject to the inequality constraints given by the yield

conditions

$$\hat{\sigma}(\hat{\boldsymbol{\mu}}) : \mathbf{m}_s^{(I)} \leq \tau_s \text{ and } \hat{\sigma}(\hat{\boldsymbol{\mu}}) : \mathbf{m}_s^{(II)} \leq \tau_s, \quad (19)$$

for all slip systems s .

It is evident from Equations (17), (18) and (19) that the disorientation axis $\boldsymbol{\mu}$ across a CBB is independent of the orientation of the CBB plane. Also, according to the Karush-Kuhn-Tucker theorem, even if certain components of $\bar{\boldsymbol{\epsilon}}$, say, $\bar{\epsilon}_{lm}$ are left unspecified, the disorientation axis, $\boldsymbol{\mu}$ can still be obtained by solving the optimization problems given by Equations (17), (18) and (19), provided the corresponding components of stress, $\hat{\sigma}_{lm} = \bar{\sigma}_{lm} = 0$.

The lower-level maximization problem is a standard linear program [32] and is solved by the simplex method. The upper-level minimization problem is non-smooth and non-linear and is solved by the section search method [34] applied over the surface of the unit sphere.

The solution to the present two level optimization problem is comprised of the deviatoric stress $\boldsymbol{\sigma}^{(I)} = \boldsymbol{\sigma}^{(II)} = \bar{\boldsymbol{\sigma}}$ in the two CBs, the slip-rates $\dot{\gamma}_s^{(I)}$ and $\dot{\gamma}_s^{(II)}$ in the slip systems $s \in \{1, 2, \dots, S\}$ of the two CBs and the optimal unit disorientation axis $\boldsymbol{\mu}$. $\dot{\gamma}_s^{(I)}$ and $\dot{\gamma}_s^{(II)}$ obtained conform to the Schmid law, Equation (7). The strain-rates, $\dot{\boldsymbol{\epsilon}}^{(I)}$ and $\dot{\boldsymbol{\epsilon}}^{(II)}$ in the two CBs can be deduced from the slip-rates using Equation (2). The orientation of the CBBs between the CBs, however, is not part of the solution of the two-level optimization problem of Equations (17) and (18); its determination requires the additional hypothesis given below.

2.5. Plastic incompatibility across the CBB: Hypothesis 3

As noted in Sections 2.3 and 2.4, while the deviatoric stress in the model grain is assumed uniform, the strain-rate exhibits a jump across CBBs. Furthermore, the deformation of CBs is generally incompatible across CBBs. In the present model, this incompatibility determines the CBB orientation. Two coordinate systems, the reference system, xyz and the CBB fixed coordinate system, XYZ , wherein the Y -axis is always aligned with the CBB normal are shown in Figure 1. In terms of strain-rates given relative to the CBB-fixed XYZ coordinate system, compatibility across the CBB [25] requires that

$$\begin{aligned} \dot{\epsilon}_{XX}^{(I)} &= \dot{\epsilon}_{XX}^{(II)}, \\ \dot{\epsilon}_{ZZ}^{(I)} &= \dot{\epsilon}_{ZZ}^{(II)} \text{ and} \\ \dot{\epsilon}_{XZ}^{(I)} &= \dot{\epsilon}_{XZ}^{(II)}. \end{aligned} \quad (20)$$

In terms of the jump in strain-rate across the CBB,

$$[[\dot{\boldsymbol{\epsilon}}]] = \dot{\boldsymbol{\epsilon}}^{(I)} - \dot{\boldsymbol{\epsilon}}^{(II)}, \quad (21)$$

the compatibility conditions, Equation (20) may be expressed as

$$[[\dot{\epsilon}_{XX}]] = [[\dot{\epsilon}_{ZZ}]] = [[\dot{\epsilon}_{XZ}]] = 0. \quad (22)$$

Violation of Equation (22) indicates incompatibility of plastic deformation in CB I and CB II across the CBB. An isotropic scalar measure of this incompatibility

is

$$\mathcal{J} = \llbracket \dot{\epsilon}_{XX} \rrbracket^2 + \llbracket \dot{\epsilon}_{YY} \rrbracket^2 + \llbracket \dot{\epsilon}_{ZZ} \rrbracket^2 + 2\llbracket \dot{\epsilon}_{XZ} \rrbracket^2. \quad (23)$$

Note that the term $\llbracket \dot{\epsilon}_{YY} \rrbracket^2$ also appears in the measure of incompatibility although compatibility in Equation (20) does not require continuity of $\dot{\epsilon}_{YY}$. This is because, according to Equations (4) and (21),

$$\llbracket \dot{\epsilon}_{YY} \rrbracket = -\llbracket \dot{\epsilon}_{XX} \rrbracket - \llbracket \dot{\epsilon}_{ZZ} \rrbracket, \quad (24)$$

which indicates the impossibility of enforcing $\llbracket \dot{\epsilon}_{XX} \rrbracket = \llbracket \dot{\epsilon}_{ZZ} \rrbracket = 0$ without also simultaneously enforcing $\llbracket \dot{\epsilon}_{YY} \rrbracket = 0$. It is now proposed that

Hypothesis 3: The CBB assumes the orientation that minimizes the incompatibility \mathcal{J} , given by Equation (23).

Hypothesis 3 thus requires the determination of a suitable orientation of the CBB fixed coordinate system XYZ relative to the global system xyz , as shown in Figure 1. Now, the Frobenius norm of the tensor $\llbracket \dot{\epsilon} \rrbracket$ is invariant with respect to coordinate rotations [35], i.e.,

$$\begin{aligned} \|\llbracket \dot{\epsilon} \rrbracket\|^2 &= \llbracket \dot{\epsilon}_{XX} \rrbracket^2 + \llbracket \dot{\epsilon}_{YY} \rrbracket^2 + \llbracket \dot{\epsilon}_{ZZ} \rrbracket^2 + 2\llbracket \dot{\epsilon}_{XY} \rrbracket^2 + 2\llbracket \dot{\epsilon}_{YZ} \rrbracket^2 + 2\llbracket \dot{\epsilon}_{XZ} \rrbracket^2 \\ &= \llbracket \dot{\epsilon}_{xx} \rrbracket^2 + \llbracket \dot{\epsilon}_{yy} \rrbracket^2 + \llbracket \dot{\epsilon}_{zz} \rrbracket^2 + 2\llbracket \dot{\epsilon}_{xy} \rrbracket^2 + 2\llbracket \dot{\epsilon}_{yz} \rrbracket^2 + 2\llbracket \dot{\epsilon}_{zx} \rrbracket^2. \end{aligned} \quad (25)$$

It follows from Equations (23) and (25) that minimization of \mathcal{J} is equivalent to maximization of

$$\mathcal{J} = \llbracket \dot{\epsilon}_{XY} \rrbracket^2 + \llbracket \dot{\epsilon}_{YZ} \rrbracket^2. \quad (26)$$

Physically, \mathcal{J} is the square of the total normal shear discontinuity across the CBB.

The Tresca yield condition of classical isotropic plasticity (e.g. [36]) requires the determination of the plane of maximum shear stress. This is analogous to the present requirement to determine the plane across which the shear strain discontinuity, \mathcal{J} , is maximized. Using this analogy, it can be seen that \mathcal{J} will be maximized provided the CBB is normal to either of the two vectors $\mathbf{v}_1 \pm \mathbf{v}_3$, where \mathbf{v}_1 and \mathbf{v}_3 denote the unit eigenvectors corresponding to the maximum and minimum eigenvalues of $\llbracket \dot{\epsilon} \rrbracket$. The two planes normal to

$$\begin{aligned} \boldsymbol{\nu}_1 &= (\mathbf{v}_1 + \mathbf{v}_3)/\sqrt{2} \text{ and} \\ \boldsymbol{\nu}_2 &= (\mathbf{v}_1 - \mathbf{v}_3)/\sqrt{2} \end{aligned} \quad (27)$$

thus satisfy Hypothesis 3. $\mathbf{v}_1 \perp \mathbf{v}_3$ implies that $\boldsymbol{\nu}_1 \perp \boldsymbol{\nu}_2$.

The two CBBs with normals $\boldsymbol{\nu}_1$ and $\boldsymbol{\nu}_2$ are distinguished based on their inclination to the primary slip plane. Without loss of generality, the CBB more closely aligned with the primary slip plane will be assigned the unit normal $\boldsymbol{\nu}_1$ and will be called CBB 1. The other CBB, normal to $\boldsymbol{\nu}_2$, will be called CBB 2. Thus, if \mathbf{n}_p denotes the normal to the primary slip plane,

$$\min(\angle\{\boldsymbol{\nu}_1, \pm\mathbf{n}_p\}) \leq \min(\angle\{\boldsymbol{\nu}_2, \pm\mathbf{n}_p\}). \quad (28)$$

2.6. **Remarks**

As noted in Section 2.1 in connection with Equation (9), Taylor's principle governs the slip activity in a grain with a uniform lattice orientation. Hypotheses 1 and 2 may be regarded as a generalization of Taylor's principle to the case of a grain with a non-uniform, but periodically repeating, lattice orientation, as shown in Figure 1. For, on the basis of minimum plastic power, as in Taylor's principle, these hypotheses provide a means to determine the optimal disorientation axis, μ , in addition to the slip rates $\dot{\gamma}_s^{(I)}$ and $\dot{\gamma}_s^{(II)}$ for $s \in \{1, 2, \dots, S\}$ in the two CBs.

Hypothesis 3, on the other hand, is similar to the LEDS principle of Kuhlmann-Wilsdorf [37]. For, elastic straining, accompanied by non-zero long-range elastic stresses [38], is required for material continuity if the plastic strains of the two CBs are incompatible. Hypothesis 3, which requires the minimization of the incompatibility of plastic strain-rates across CBBs thus amounts to requiring minimization of the long-range stresses produced by CBBs, as demanded by the LEDS principle.

The three present hypotheses are now compared with the hypotheses underlying some of the models available in the literature. Chin and Wonsiewicz [39] proposed that deformation banding, i.e., inhomogeneous deformation of a grain, will result if the plastic power required for the inhomogeneous process is smaller than the plastic power required for the homogeneous process¹. The inhomogeneous plastic power is the sum of the power associated with plastic deformation of bands, the energy-rate associated with band boundaries and the plastic power required to correct shape differences between the banded and homogeneous deformation. Chin and Wonsiewicz assumed constant lattice orientation and slip system hardness during both inhomogeneous and homogeneous deformations. Thus, inhomogeneous deformation of grains, according to the Chin-Wonsiewicz criterion, is not caused by slip system hardening. The Chin-Wonsiewicz criterion has been extended and applied to rolling deformation by Lee and Duggan [40].

A variational theory for the inhomogeneous deformation and accompanying sub-division of a single crystal under imposed homogeneous deformation has been proposed by Ortiz and co-workers [41, 42]. According to this theory, a non-homogeneous deformation mode will be preferred if a functional comprised of the plastic work and the stored energy associated with the geometrically necessary interfaces during inhomogeneous deformation is non-convex. In that case, the functional will be minimized by an inhomogeneous deformation accompanied by sub-structure development. Crystal sub-division occurs within this framework because plastic work can be reduced by lowering latent hardening, which in turn can happen if multi-slip activity in a homogeneously deforming crystal is replaced with single slip activity within spatially isolated domains. The approach of Hackl and co-workers [43, 44] to predicting microstructure formation is similar. In their thermodynamics-based approach, which may qualitatively be regarded as a rigorous extension of the LEDS theory of Kuhlmann-Wilsdorf [37], a free energy functional representing the stored energy due to elastic deformation is minimized. Non-convexity of the functional leads to inhomogeneous deformation and microstructure formation, as in [41, 42]. The reduction in the number of slip systems activated in each CB of an inhomogeneously deforming grain, relative to the number that must be activated in the course of homogeneous deformation of the grain has also been taken by Leffers [30, 45] to underlie experimentally observed sub-structure in grains.

The theory of Ortiz and co-workers [46, 47] is able to predict the scaling of misorientation angle and the spacing of microstructural boundaries, in accord with

¹Chin and Wonsiewicz [39] require the minimization of plastic work over an infinitesimal plastic strain increment, which amounts to requiring the minimization of the plastic power.

experimental observations, when infinite latent hardening is assumed. However, the orientations and disorientation axes across microstructural boundaries predicted by the aforementioned theories have not been systematically compared with experimental observations.

Hypotheses 1 and 2 of the present model are more akin to the Chin-Wonsiewicz criterion [39] than to the criteria of [41–44]. The inhomogeneous deformation mode predicted by Hypotheses 1 and 2 is based on minimization of the instantaneous plastic power, P_1 , given by Equation (15) and is, therefore, independent of slip system hardening. As noted above, the criteria of [41–44] predict inhomogeneous grain deformation on the basis of a tendency to minimize latent hardening of slip systems. However, the present hypotheses differ also from those given by [39, 40] in two significant ways: (i) CBs in the present hypotheses, unlike those in [39, 40], are assumed disorientated. (ii) CBB orientations are determined on the basis of Hypothesis 3 presently, instead of being prescribed based on geometric considerations, as in [39, 40].

2.7. Dislocation density and disorientation angle

The rate of change of the dislocation density tensor, α associated with the CBB and the rate of change of the disorientation angle, ω of the CBB are now derived. Let α^V denote the volumetric dislocation density tensor; its components describe the dislocation line length per unit material volume. Following Fleck et al. [48], the rate of α^V is given by

$$\dot{\alpha}^V = \nabla \times \mathbf{L}_{ss}, \tag{29}$$

or, in component form, $\dot{\alpha}_{in}^V = e_{nkj} L_{ss\ ij,k}$, where, e_{nkj} are the components of the alternating tensor. Let $\mathbf{L}_{ss}^{(I)}$ and $\mathbf{L}_{ss}^{(II)}$ denote the uniform slip rate tensors in CB I and CB II , respectively. According to Equation (29), $\dot{\alpha}^V = \mathbf{0}$ in the domain of the two CBs. Let α denote the surface dislocation density tensor associated with CBBs, whose components represent the dislocation line length per unit CBB surface area. Its rate, $\dot{\alpha}$ is given by [41, 42]

$$\dot{\alpha} = \llbracket \mathbf{L}_{ss} \rrbracket \times \nu, \tag{30}$$

where, $\llbracket \mathbf{L}_{ss} \rrbracket = \mathbf{L}_{ss}^{(I)} - \mathbf{L}_{ss}^{(II)}$. In component form, $\dot{\alpha}_{in} = e_{nkj} \llbracket L_{ss\ ij} \rrbracket \nu_k$. Following Nye [49], the relation between $\dot{\alpha}$ and the network of dislocations is

$$\dot{\alpha} = \sum_{t=1}^T \dot{\rho}^{(t)} b \mathbf{b}^{(t)} \otimes \boldsymbol{\xi}^{(t)}, \tag{31}$$

where the summation is over all the dislocation types $t = 1, \dots, T$. In Equation (31), $\dot{\rho}^{(t)}$ denotes the areal density, i.e., dislocation line length per unit CBB surface area, of dislocation of type t , b denotes the magnitude of the Burgers vector and $\mathbf{b}^{(t)}$ and $\boldsymbol{\xi}^{(t)}$ denote unit vectors in the direction of the Burgers vector and the line direction of dislocations of type t , respectively. The scalar rate of the geometrically necessary dislocation density may be defined following Sun et al. [50] as:

$$\dot{\rho}_{\text{GND}} = \sum_{t=1}^T \dot{\rho}^{(t)}. \tag{32}$$

Using the relation between the lattice curvature and dislocation density due to Nye [49],

$$\dot{\boldsymbol{\kappa}} = \dot{\boldsymbol{\alpha}}^T - (\text{tr } \boldsymbol{\alpha})\mathbf{1}/2, \quad (33)$$

where $\mathbf{1}$ denotes the second rank identity tensor, the rate of change of the vector lattice orientation, $\dot{\boldsymbol{\phi}}$ across the CBB can be obtained as

$$\dot{\boldsymbol{\phi}} = \dot{\boldsymbol{\kappa}}\boldsymbol{\nu}. \quad (34)$$

The disorientation rate across the CBB, $\dot{\omega}$ is then

$$\dot{\omega} = \|\dot{\boldsymbol{\phi}}\| = \sqrt{\dot{\boldsymbol{\phi}} \cdot \dot{\boldsymbol{\phi}}}. \quad (35)$$

Substituting Equations (30), (33) and (34) into Equation (35), followed by algebraic manipulations yields

$$\dot{\omega} = \sqrt{\|\boldsymbol{\nu} \times (\llbracket \mathbf{L}_{ss}^T \rrbracket \boldsymbol{\nu})\|^2 + (\boldsymbol{\nu} \cdot \text{axial skew}(\llbracket \mathbf{L}_{ss} \rrbracket))^2}. \quad (36)$$

3. Results and discussion

We now predict the disorientation axis $\boldsymbol{\mu}$ and orientations $\boldsymbol{\nu}_1$ and $\boldsymbol{\nu}_2$ of CBBs formed in the grains of an fcc polycrystal accommodating imposed uniaxial tensile deformation along the z axis by $\{111\}\langle 110 \rangle$ slip. 600 grains are analyzed. Their lattice orientations fall in a regular grid within the standard stereographic triangle whose vertices correspond to the $[001]$, $[011]$ and $[111]$ crystallographic directions, i.e., the tensile axis, z , is collinear with a crystallographic direction given by $\alpha[001] + \beta[011] + \gamma[111]$, for some $\alpha \geq 0$, $\beta \geq 0$ and $\gamma \geq 0$. For grains oriented within this stereographic triangle, the primary, conjugate, cross and critical slip planes, as defined, e.g., in [51, Section 5.16], are $\mathbf{n}_p = (\bar{1}11)$, $\mathbf{n}_c = (1\bar{1}1)$, $\mathbf{n}_x = (11\bar{1})$ and $\mathbf{n}_r = (111)$, respectively. The only material parameter in the present model is the critical resolved shear stress of all slip systems; these are taken to be equal:

$$\tau_s = 1 \quad \text{for } s \in \{1, 2, \dots, 12\}, \quad (37)$$

without loss of generality.

3.1. Constraints

The constraint experienced by an individual grain in a polycrystal is mediated by the grains surrounding it and will, in general, differ from the macroscopic constraint imposed upon the polycrystal [25]. In the present work, the constraints imposed upon a grain in a polycrystal undergoing uniaxial tension in the z -direction are

$$\begin{aligned} \bar{\epsilon}_{zz} &= 1, \\ \bar{\epsilon}_{xx} + \bar{\epsilon}_{yy} &= -1, \\ \bar{\epsilon}_{xz} = \bar{\epsilon}_{yz} = \bar{\epsilon}_{zx} = \bar{\epsilon}_{zy} &= 0. \end{aligned} \quad (38)$$

$\bar{\epsilon}_{xx}$ and $\bar{\epsilon}_{yy}$ are thus only partially constrained and $\bar{\epsilon}_{xy} = \bar{\epsilon}_{yx}$ are left unconstrained.

This set of constraints is motivated by the viscoplastic self-consistent polycrystal plasticity model [25, Chap. 11, p. 484], which predicts that individual grains in a polycrystal **subjected to macroscopic uniaxial tension** undergo approximately plane strain deformation **due to grain curling**. Plane strain deformation involves extension in a certain direction and equal contraction in a perpendicular direction. The strain-rate in a grain undergoing plane strain deformation with extension along the z -direction and compression along an arbitrary unit direction $(\xi, \pm\sqrt{1-\xi^2}, 0)$ perpendicular to the z -direction can be shown to be

$$[\bar{\dot{\epsilon}}]_{xyz} = \begin{pmatrix} -\xi^2 & \mp\xi\sqrt{1-\xi^2} & 0 \\ \mp\xi\sqrt{1-\xi^2} & -(1-\xi^2) & 0 \\ 0 & 0 & 1 \end{pmatrix}, \quad (39)$$

for arbitrary ξ , $0 \leq \xi \leq 1$. In terms of components, Equation (39) can be written as

$$\begin{aligned} \bar{\dot{\epsilon}}_{zz} &= 1, \\ \bar{\dot{\epsilon}}_{xx} + \bar{\dot{\epsilon}}_{yy} &= -1, \\ \bar{\dot{\epsilon}}_{xz} = \bar{\dot{\epsilon}}_{yz} = \bar{\dot{\epsilon}}_{zx} = \bar{\dot{\epsilon}}_{zy} &= 0, \\ \bar{\dot{\epsilon}}_{xy} = \bar{\dot{\epsilon}}_{yx} &= \mp\sqrt{|\bar{\dot{\epsilon}}_{xx}\bar{\dot{\epsilon}}_{yy}|}. \end{aligned} \quad (40)$$

It is thus seen that the imposed constraints listed in Equation (38) are exactly those required to enforce plane strain deformation of the grain given in Equation (40), with the omission of the last non-linear constraint in Equation (40). The deviation from plane strain deformation caused by the omission of the last constraint is studied below.

3.2. Homogeneous deformation

If the disorientation between neighboring CBs in the model grain described in Section 2.2, $\omega = 0$, both CBs slip identically and the grain deforms homogeneously. The plane strain character of the homogeneous deformation and the concentration of slip activity in a single crystallographic slip plane are now considered.

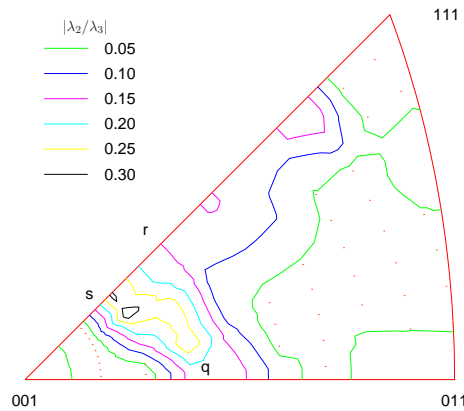


Figure 2. Contour map over the standard stereographic triangle of $|\lambda_2/\lambda_3|$, the ratio of the intermediate eigenvalue to the maximum eigenvalue of the strain-rate imposed on the grain, $\dot{\epsilon}$, which quantifies the deviation of the grain deformation from plane strain deformation. Equal angle projection is assumed.

Let $\bar{\epsilon}$ denote the strain-rate of a grain whose CBs are identically oriented and which is homogeneously deforming ($\dot{\epsilon}^{(I)} = \dot{\epsilon}^{(II)} = \bar{\epsilon}$) under the imposed constraint given by Equation (38). Let λ_1, λ_2 and λ_3 denote the eigenvalues of $\bar{\epsilon}$ ordered as $\lambda_1 \leq \lambda_2 \leq \lambda_3$. A measure of the deviation of $\bar{\epsilon}$ from plane strain deformation is given by $|\lambda_2/\lambda_3|$. For plane strain deformation, $|\lambda_2/\lambda_3| = 0$, while for axisymmetric uniaxial tension, $|\lambda_2/\lambda_3| = 0.5$. Figure 2 shows the variation of $|\lambda_2/\lambda_3|$ over the stereographic triangle. It is seen that in both the main part of the triangle and close to the [001], [011] and [111] poles, $|\lambda_2/\lambda_3| \leq 0.2$, which indicates the plane strain character of $\bar{\epsilon}$ to good approximation. In the region qrs of the stereographic triangle of Figure 2, however, $0.2 \leq |\lambda_2/\lambda_3| \leq 0.34$. In this region, the grain deformation deviates more significantly from plane strain, although here too, the grain deformation falls distinctly short of having the character of axisymmetric uniaxial tension.

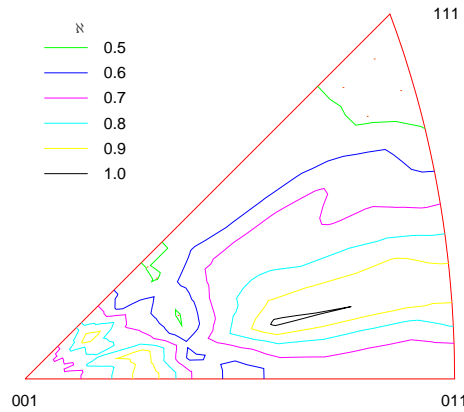


Figure 3. Contour map of \aleph , defined in Equation (41), which quantifies concentration of slip in a single $\{111\}$ plane. Equal angle projection is assumed.

The concentration of slip activity in one crystallographic slip plane in a homogeneously deforming grain is considered next. Let $\dot{\Gamma}_p$ denote the sum of the slip rates $\dot{\gamma}_s$ for slip systems s associated with the primary slip plane when the disorientation angle across CBBs, $\omega = 0$, as in Equation (6). $\dot{\Gamma}_c, \dot{\Gamma}_x$ and $\dot{\Gamma}_r$, for total slip activity in the conjugate, cross and critical planes, respectively, may similarly be defined. The ratio

$$\aleph = \frac{\max_{i \in \{p,c,x,r\}} \dot{\Gamma}_i}{\sum_{i \in \{p,c,x,r\}} \dot{\Gamma}_i}; \tag{41}$$

$1/4 \leq \aleph \leq 1$ quantifies the concentration of slip activity in one $\{111\}$ plane. The lower bound, $\aleph = 1/4$, signifies that slip activity is uniformly distributed amongst all slip planes while the upper bound, $\aleph = 1$, signifies concentration of slip activity in one plane. Figure 3 shows the contours of \aleph over the stereographic triangle. It is seen that the highest \aleph , i.e., greatest slip concentration in one $\{111\}$ plane, occurs in grains oriented in the middle part of the triangle.

3.3. Inhomogeneous deformation

The following discussion is based on the model of Section 2.2 wherein grains are assumed to be subdivided by a repetitive pattern of two types of mutually disoriented CBs, separated by CBBs. The disorientation between the CBs, $\omega \neq 0$.

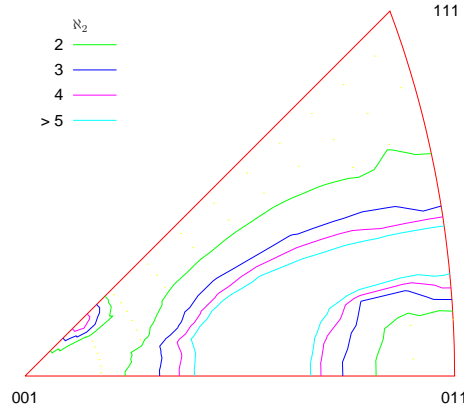


Figure 4. Contour map over the standard stereographic triangle of \aleph_2 , given by Equation (42), which quantifies the ratio of slip activity in the CBs. $\aleph_2 = 1$ implies equal total slip rate in both CBs, while $\aleph_2 = \infty$ implies concentration of slip in one of the two CBs. Equal angle projection is assumed.

3.3.1. Slip activity in CBs

The distribution of slip activity in each of the two types of CBs is first considered. A measure of the concentration of slip activity in one of the CBs is given by

$$\aleph_2 = \frac{\max \left(\sum_{i \in \{p,c,x,r\}} \dot{\Gamma}_i^{(I)}, \sum_{i \in \{p,c,x,r\}} \dot{\Gamma}_i^{(II)} \right)}{\min \left(\sum_{i \in \{p,c,x,r\}} \dot{\Gamma}_i^{(I)}, \sum_{i \in \{p,c,x,r\}} \dot{\Gamma}_i^{(II)} \right)}. \quad (42)$$

It is clear that $1 \leq \aleph_2 < \infty$. $\aleph_2 = 1$ implies equal distribution of slip activity amongst both types of CBs, while $\aleph_2 = \infty$ implies that only one of the two model rigid-plastic CBs undergoes plastic deformation, while the other remains rigid.

Figure 4 shows the contours of \aleph_2 over the standard stereographic triangle. While slip activity and plastic deformation of both CBs is predicted in orientations close to the [001], [011] and [111] corners of the triangle and all along the [001]-[111] line, concentration of slip activity in one of the CBs is predicted in the middle part of the triangle, corresponding to $\aleph_2 > 5$.

3.3.2. Alignment of CBBs with {111} planes

Let θ_1^{\min} and θ_2^{\min} denote the smallest angular misalignment of CBB 1 and CBB 2 with any of the crystallographic planes, i.e.,

$$\begin{aligned} \theta_1^{\min} &= \min_{i \in \{p,c,x,r\}} (\angle \{ \nu_1, \pm \mathbf{n}_i \}) \text{ and} \\ \theta_2^{\min} &= \min_{i \in \{p,c,x,r\}} (\angle \{ \nu_2, \pm \mathbf{n}_i \}). \end{aligned} \quad (43)$$

Figures 5(a) and (b) show the predicted deviation, θ_1^{\min} and θ_2^{\min} , of CBB 1 and CBB 2, respectively, from the nearest {111} plane and disoriented by $\omega = 0.32^\circ$. If this lattice disorientation is introduced by statistically stored dislocations, the average lattice disorientation scales with von Mises strain as [31]

$$\langle |\omega| \rangle = k \sqrt{\epsilon_{vM}}, \quad (44)$$

where $k = 1^\circ$ for aluminum. According to Equation (44), the disorientation angle $\omega = 0.32^\circ$ corresponds to von Mises strain-level $\epsilon_{vM} = 0.1$. Figure 5 (a) predicts close coincidence of CBB 1 with a {111} plane in the middle part of the stereographic triangle, labeled *abcd*. Coincidence to within $\theta_2^{\min} \leq 15^\circ$ between CBB 2

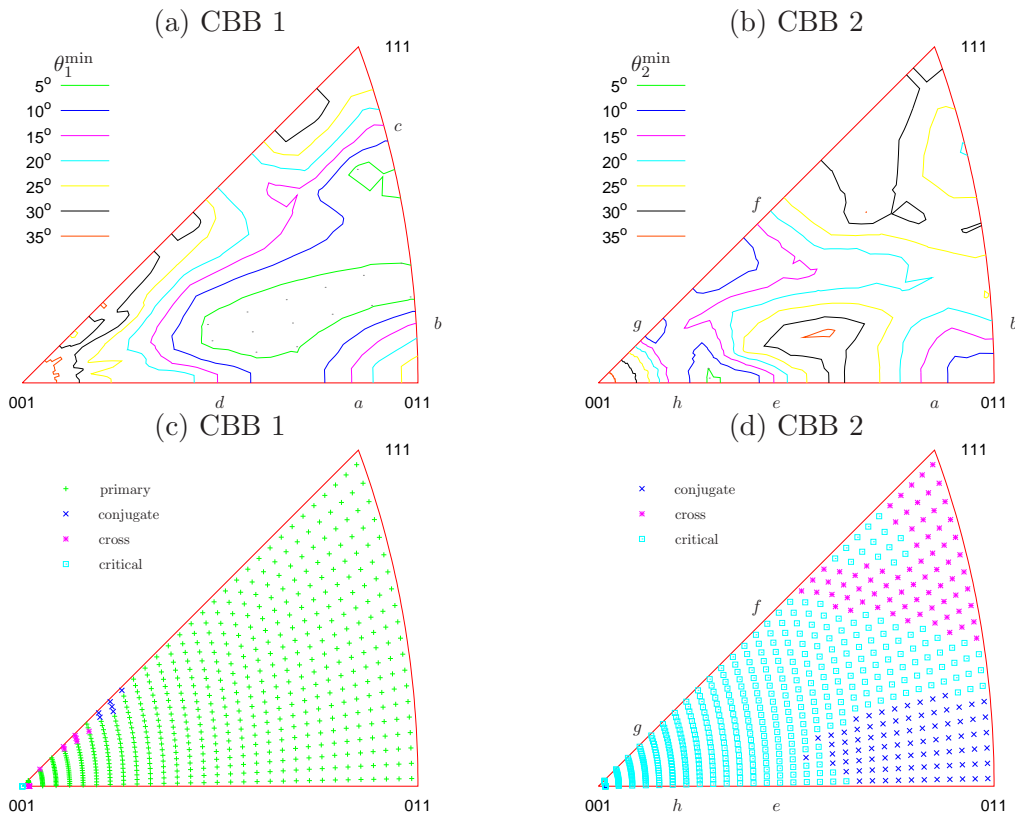


Figure 5. Inverse pole figures drawn using equal angle projection showing contours of (a) θ_1^{\min} and (b) θ_2^{\min} corresponding to strain level $\epsilon_{\text{VM}} = 0.1$. The $\{111\}$ plane most closely aligned with CBB 1 and CBB 2 is shown in (c) and (d), respectively.

and a $\{111\}$ plane is also predicted in the part of the stereographic triangle labeled $efgh$ and in region $a[011]b$ near the $[011]$ pole, as shown in Figure 5(b).

The $\{111\}$ planes most closely aligned with CBB 1 and CBB 2 are shown in Figures 5(c) and (d). As seen from Figure 5(c), excepting small regions of the orientation space near the $[001] - [111]$ line, CBB 1 predominantly aligns most closely with the primary slip plane, even in parts of the stereographic triangle where θ_1^{\min} is large. On the other hand, in the part of orientation space, $efgh$, where there is close CBB 2 alignment with a $\{111\}$ plane, it is seen from Figure 5(d) that the $\{111\}$ planes best aligned with CBB 2 are the critical slip planes.

The region of close alignment of CBB 1 with a $\{111\}$ plane occurs for grain orientations wherein the imposed tensile deformation is accommodated predominantly by slip in a single crystallographic plane. The region of the stereographic triangle in Figure 5 (a) corresponding to good alignment of CBB 1 with a $\{111\}$ plane to within $\theta_1^{\min} \leq 10^\circ$, say, is approximately the same as the region of the triangle in Figure 3 corresponding to high \aleph , $\aleph \geq 0.7$, approximately. Parts of the region of small θ_2^{\min} in Figure 5(b), however, maps to a region of relatively small slip concentration \aleph in Figure 3. The region of close coincidence of CBB 1 with a $\{111\}$ plane is also approximately the same as the region of large \aleph_2 in Figure 4. Thus, deformation is predominantly confined to one of the CBs in grain orientations for which θ_1^{\min} is small. Deformation is more equitably distributed amongst the CBs for grain orientations for which θ_2^{\min} is small.

3.3.3. Insensitivity of CBB orientation to strain level

Figure 6 shows the lattice orientation dependence of θ_1^{\min} and θ_2^{\min} for the strain level $\epsilon_{\text{VM}} = 0.01$, which corresponds to $\omega = 0.1^\circ$ according to Equation (44). Only

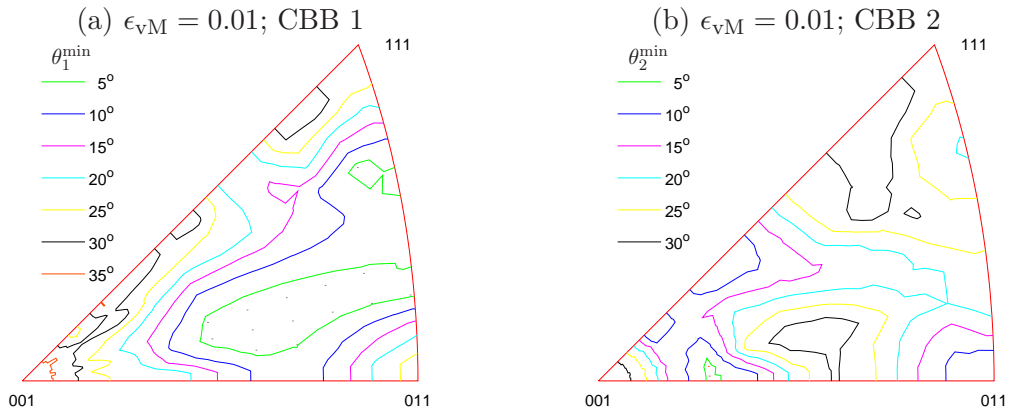


Figure 6. Inverse pole figures drawn using equal angle projection showing contours of (a) θ_1^{\min} and (b) θ_2^{\min} at $\epsilon_{vM} = 0.01$.

a slight difference is seen between (a) and (b) of this figure and Figures 5(a) and (b), respectively. This suggests that CBB orientation predictions are not sensitive to the strain level at least in the strain range $\epsilon_{vM} = 0.01$ to 0.1. **The predicted insensitivity can be understood in the context of the present model by noting that the distribution of slip activity is not altered significantly by small variations in the disorientation angle across the CBBs, so that the strain-rates, $\dot{\epsilon}^{(I)}$ and $\dot{\epsilon}^{(II)}$, of CBs and the CBB orientation are also left practically unaltered.** The predicted insensitivity agrees well with experimental findings [11, 13, 19].

3.3.4. Tilt/twist character of the predicted CBBs

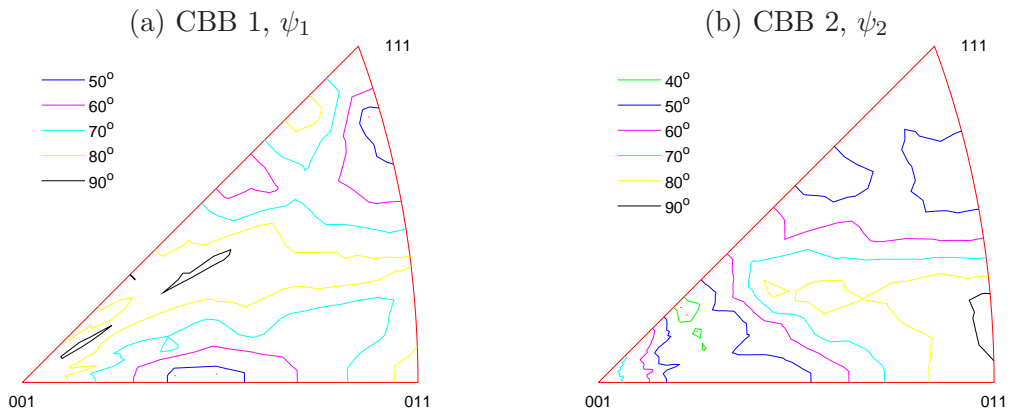


Figure 7. Inverse pole figures drawn using equal angle projection showing contours of (a) ψ_1 and (b) ψ_2 . $\epsilon_{vM} = 0.1$.

The tilt/twist character of the predicted CBBs for each of the 600 orientations considered can be ascertained by considering the acute angle included between the CBB disorientation axis, $\boldsymbol{\mu}$ and the CBB normal, $\boldsymbol{\nu}_1$ or $\boldsymbol{\nu}_2$. These angles are

$$\psi_1 = \min(\angle\{\pm\boldsymbol{\mu}, \boldsymbol{\nu}_1\}) \text{ and } \psi_2 = \min(\angle\{\pm\boldsymbol{\mu}, \boldsymbol{\nu}_2\}). \quad (45)$$

$0 \leq \psi_1, \psi_2 \leq 90^\circ$. $\psi_1 \approx 0^\circ$ or $\psi_2 \approx 0^\circ$ indicates that that the boundary has a predominantly twist character, while $\psi_1 \approx 90^\circ$ or $\psi_2 \approx 90^\circ$ indicates a predominantly tilt CBB. Figures 7 (a) and (b) show the distribution of ψ_1 and ψ_2 , respectively, over the entire orientation space. It is striking that there are no orientations for which ψ_1 or ψ_2 is smaller than 40° . Thus, the present calculations predict no predominantly twist CBBs anywhere in the orientation space. On the other hand,

Figure 7(a) shows that CBB 1s in much of the stereographic triangle, barring some regions near the $[001]$ – $[011]$, $[011]$ – $[111]$ and $[111]$ – $[001]$ lines, have a predominantly tilt character, corresponding to $\psi_1 \geq 70^\circ$. Parts of the region, labeled $abcd$ in Figure 5 (a), where CBB 1 coincides closely with the primary slip plane thus have CBBs with a predominantly tilt character, while other parts have CBBs with mixed character. Also, it can be seen from Figure 7(b) that the part of the stereographic triangle where CBB 2 has a predominantly tilt character ($\psi_2 \geq 70^\circ$) occurs only in the middle of the triangle. In the part of the orientation space, $efgh$ in Figure 5 (b), where CBB 2 aligns closely with a crystallographic $\{111\}$ plane, this CBB is of mixed type.

Not as much experimental data for the distribution of CBB disorientation axes as for the distribution of CBB orientation is available for the case of polycrystals deformed in uniaxial tension. Data is, however, available for the character of CBBs in rolled polycrystals [52] at low rolling reductions. McCabe et al [52] have reported the predominantly tilt character of a crystallographic CBB (disorientation axis tilted 69° relative to the CBB normal) within a grain of a pure copper polycrystal reduced 7.5% by rolling. As noted in Section 3.3.2, crystallographic CBBs occur in the central part of the stereographic triangle under uniaxial tension. In this region of orientation space, Figure 7 (a) predicts predominantly tilt CBB.

3.3.5. Dislocation density

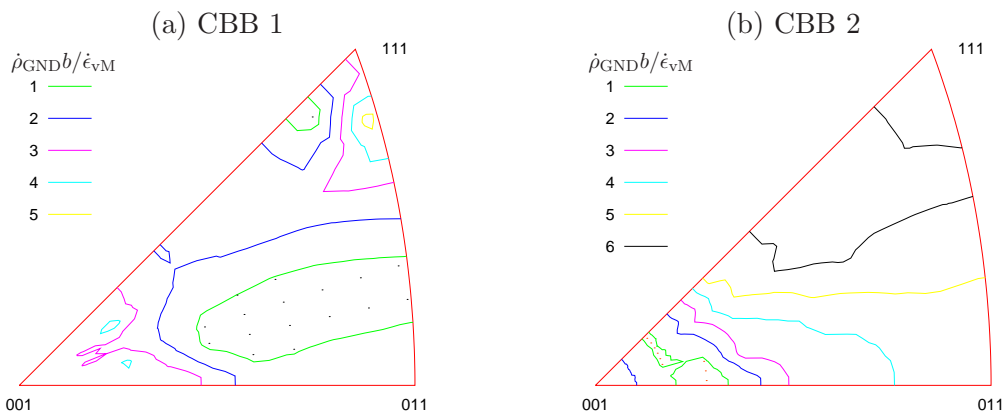


Figure 8. Inverse pole figures drawn using equal angle projection showing contours of non-dimensional $\rho_{\text{GND}}b/\dot{\epsilon}_{\text{VM}}$ in (a) CBB 1 and (b) CBB 2 at $\epsilon_{\text{VM}} = 0.1$. b denotes the magnitude of the Burgers vector.

Following Sun et al. [50], it is assumed that plastic deformation of an f.c.c. grain deforming by $\{111\}\langle 110 \rangle$ slip is accommodated by the motion of 12 types of pure screw dislocations, whose Burgers vectors and line directions are aligned along the $\langle 110 \rangle$ directions and 24 types of pure edge dislocations whose Burgers vector lie along $\langle 110 \rangle$ and whose line directions along $\langle 112 \rangle$. A decomposition of the 9 components of $\dot{\alpha}$ into dislocation density rates, $\dot{\rho}^{(t)}$, $t = 1, 2, \dots, T$, for $T = 12 + 24 = 36$ dislocation types in Equation (31) constitutes an underdetermined problem. The lower-bound f.c.c. deconstruction of Sun et al. [50], which provides a method to handle the indeterminacy, is employed presently for the determination of $\dot{\rho}^{(t)}$.

Figure 8 shows the lattice orientation dependence of the non-dimensional $\rho_{\text{GND}}b/\dot{\epsilon}_{\text{VM}}$, given by Equation (32), across CBB 1 and CBB 2. Comparing Figures 8 (a) and (b) with Figures 5 (a) and (b) shows that CBBs aligned closely with a $\{111\}$ plane have the smallest rates of dislocation density accumulation. However, smallness of $\rho_{\text{GND}}b/\dot{\epsilon}_{\text{VM}}$ does not necessarily imply close coincidence of the predicted CBB with a $\{111\}$ plane: Orientations for which $\rho_{\text{GND}}b/\dot{\epsilon}_{\text{VM}}$ is small,

but for which the predicted CBB 1 deviates significantly from $\{111\}$ planes occur fall the $[433]$ pole. The highest $\dot{\rho}_{\text{GND}}b/\dot{\epsilon}_{\text{VM}}$ is associated with CBB 2s in grains oriented near the $[111]$ pole.

3.3.6. Disorientation angle

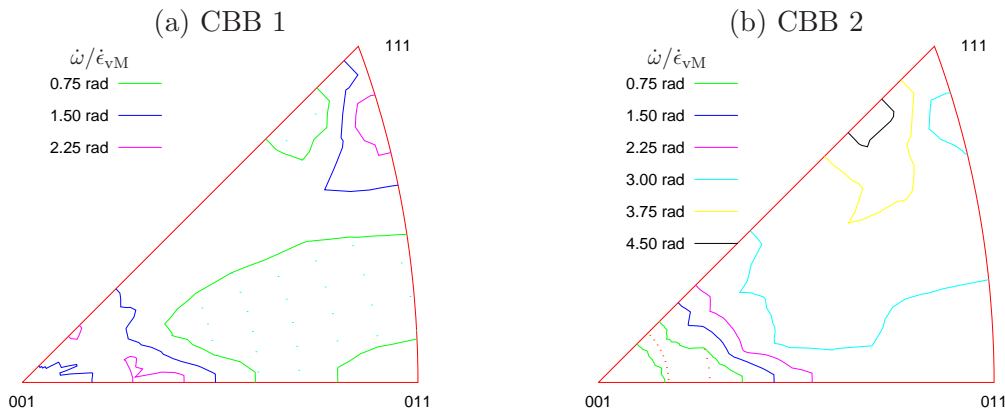


Figure 9. Inverse pole figures drawn using equal angle projection showing contours of $\dot{\omega}/\dot{\epsilon}_{\text{VM}}$ in (a) CBB 1 and (b) CBB 2 at $\epsilon_{\text{VM}} = 0.1$.

Figure 9 shows the lattice orientation dependence of the non-dimensional disorientation angle rate, $\dot{\omega}/\dot{\epsilon}_{\text{VM}}$, defined in Section 2.7, across CBB 1 and CBB 2. The value of $\dot{\omega}/\dot{\epsilon}_{\text{VM}}$ across CBB 1 in Figure 9 (a) averaged over the entire stereographic triangle, 0.98 rad, is smaller than the average value, 2.95 rad, across CBB 2 in Figure 9 (b). Furthermore, comparison of Figure 9 with Figure 5 (a) and (b) shows that the lattice orientations for which either CBB 1 or CBB 2 coincide closely with a $\{111\}$ plane approximately correspond to small values of $\dot{\omega}/\dot{\epsilon}_{\text{VM}}$.

Figure 9 corresponds to a strain-level of $\epsilon_{\text{VM}} = 0.1$, i.e., a disorientation angle of $\omega = 0.32^\circ$, according to Equation (44). The distribution of $\dot{\omega}/\dot{\epsilon}_{\text{VM}}$ over the stereographic triangle shown in Figure 9 does not, however, appreciably vary with ω at least up until $\omega = 2^\circ$. If the lattice orientations of grains were fixed, this observation would imply that the predicted disorientation angle ω across a CBB scales linearly with strain, ϵ_{VM} . But, the lattice orientation of grains evolves during tensile deformation, following a path in the stereographic triangle [53]. The disorientation angle, ω at the end of the deformation is predicted to be the integral of the non-constant $\dot{\omega}$ over the path describing it.

Evolution of the disorientation angle with lattice rotation is deferred to future work. Predicted microstructural features associated with the instantaneous distribution of slip activity in a grain, viz., CBB ν and μ are now compared with experimental observations.

3.4. Comparison with experimental observations

Extensive experimental studies of the crystallographic alignment of CBBs have been conducted in polycrystalline copper and aluminum subjected to uniaxial tensile deformation [11–13, 15, 18, 19, 21]. In the experimental observations, CBBs are found to be comprised of discontinuous segments separated by step like discontinuities [19]. The crystallographic plane of a CBB has been experimentally identified by measuring the crystallographic orientation of a few of continuous CBB segments in several grains, as detailed by Huang and Winther [19].

The gross orientation of a CBB is the orientation of the single plane that best fits all the dislocation segments comprising it. The distinction between the crystal-

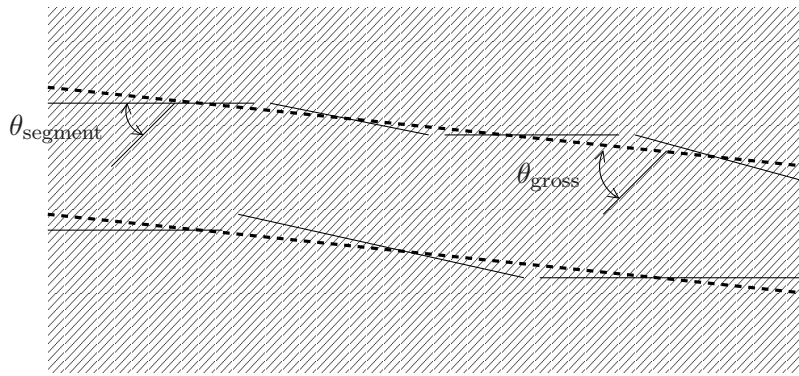


Figure 10. Schematic diagram showing the distinction between the orientation of individual continuous segments comprising the CBB (solid lines) and the gross orientation of the CBB averaged over the entire grain (dashed line). The diagonal lines in the background represent the average lattice orientation of the grain.

lographic orientation of individual CBB segments and the gross CBB orientation is illustrated schematically in Figure 10. The inclination of a CBB segment to a certain crystallographic plane and the inclination of the gross CBB to that plane have been indicated as θ_{segment} and θ_{gross} , respectively. It is clear that $\theta_{\text{segment}} \neq \theta_{\text{gross}}$. The present model predicts the gross CBB orientation, since it treats the CBB as a planar boundary devoid of any discontinuities.

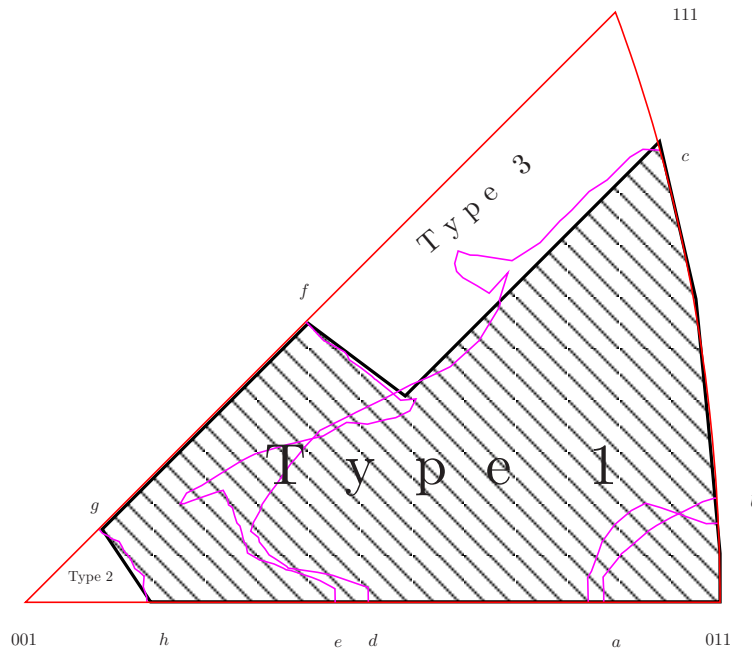


Figure 11. Division of the stereographic triangle into Type 1, Type 2 and Type 3 regions based on the present calculations. Regions $abcd$ and $efgh$ are the same as those marked in Figures 5(a) and (b), respectively. Contour lines shown correspond to those of $\theta_1^{\text{min}} = 15^\circ$ and $\theta_2^{\text{min}} = 15^\circ$ in Figures 5(a) and (b), respectively.

A division of the orientation space, following Huang [11], obtained on the basis of the present calculations is shown in Figure 11. In the Type 1 region obtained as the union of the regions $abcd \cup efgh \cup a[011]b$, shown in Figure 5, the gross orientation of CBBs aligns to within 15° with a crystallographic slip plane. It is seen that a part of the contour line cd overlaps approximately with a part of the contour line ef . The Type 2 region is characterized by the unstable CBBs, while the Type 3 region is characterized by stable non-crystallographic CBBs. Detailed discussion of each of the three types follows.

3.4.1. Type 1 grains

Huang and Hansen [11] observed CBBs aligned with $\{111\}$ planes in the middle part of the triangle, and termed such grains as Type 1 grains. The characteristic crystallographic CBBs of Type 1 grains have since been found in copper and aluminum of varying purity, grain size and strain levels [13, 16, 18–21]. In these works, the angle between the CBB segments and the $\{111\}$ plane is reported to be less than 10° , and even as close as 5° [11, 13]. Winther et al. [15] and Huang and Winther [19] have reported that CBB segments in Type 1 grains usually align with the primary slip plane, although for Type 1 grains oriented near the $[001]$ corner they may align with the conjugate or critical $\{111\}$ planes.

In reasonable agreement with these experimental observations, Figure 5(a) shows that the predicted CBB 1 aligns with the primary $\{111\}$ plane to within 15° in the middle part of the triangle, denoted by $abcd$, as shown in Figure 5 (b). Also, the predicted CBB 2 aligns closely with the critical slip plane in the region $efgh$ shown in Figure 5 (d). It is also seen in the same figure that in region $a[011]b$, the predicted CBB 2 aligns closely with conjugate plane.

Figure 11 shows the region $abcd \cup efgh \cup a[011]b$, which corresponds to the calculated Type 1 region. The calculated Type 1 region agrees well with the experimentally observed Type 1 region of Huang, Winther and co-workers [13, 16, 18–21].

The observed agreement of the predicted and experimental CBB alignments are found even though, as noted at the beginning of Section 3.4, it is the crystallographic orientation of CBB segments that is experimentally measured, while it is the gross crystallographic CBB orientation that is predicted. This is perhaps because in Type 1 grains, the orientation relation of CBB segments to the lattice is approximately the same as the gross orientation of the CBB to the lattice.

Although the present model predicts two sets of mutually orthogonal CBBs for each lattice orientation, except in rare cases [11, 21], only one set of CBBs is reported from experimental observations. This indicates a microscopic preference for one of the predicted CBB orientations. Figure 8 suggests that the Type 1 CBB observed experimentally is that corresponding to the smaller $\dot{\rho}_{\text{GND}b}/\dot{\epsilon}_{\text{VM}}$. Another reason for the observed single CBB in Type 1 grains has been suggested by Winther et al [15]. It holds that CBB formation requires dislocations from at least two coplanar systems. The unavailability of sufficiently many suitable dislocations to form both CBBs may be the reason for the observed absence of two CBBs.

3.4.2. Type 2 grains

In the region close to the $[001]$ pole, Huang, Winther and co-workers [11, 13, 16, 18–21] have observed a diffuse cell structure instead of CBBs. Such grains have been called Type 2 grains. The present model is unable to directly predict the breakdown of the CBB structure. In fact, as seen in Figures 5 (a) and (b), the present model predicts CBBs deviating substantially from any $\{111\}$ planes in the part of the orientation space near the $[001]$ pole.

The present results, however, indirectly suggest the impersistence of the predicted CBBs in Type 2 grains. The irregularity of the contour line nearest the $[001]$ pole in Figure 5 (a) and the high density of contours near the $[001]$ pole in Figure 5 (b) suggests that the predicted CBB orientations are highly sensitive to the lattice orientation of grains oriented with tensile axis near the $[001]$ pole. This is more clearly seen in Figure 12, which shows a large scatter in the orientation of the predicted CBBs in 40 orientations near the $[001]$ pole, for which the crystallographic $[001]$ direction deviates from the tensile z -axis by less than 6° . For grains of these orientations, one set of predicted CBBs are oriented from (100) to $(\bar{1}10)$ and another set of predicted CBBs from (001) to (011) . The variation of the CBB orientation

in both sets is slightly over 45° . It is proposed that the CBBs predicted in Type 2 grains do not persist with deformation because large changes in the optimal CBB orientation accompany relatively small lattice rotations, such as those that occur during deformation [21]. This may be the underlying reason for the experimentally observed absence of CBBs in Type 2 grains.

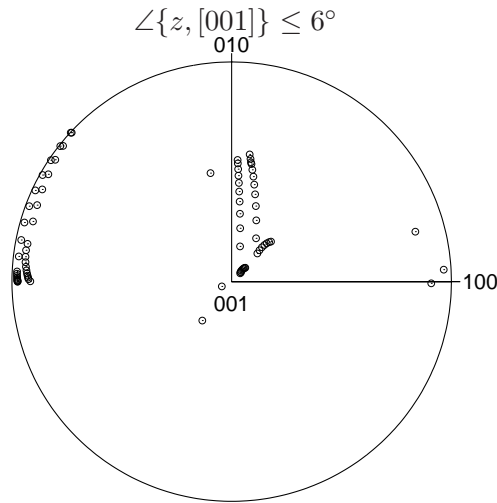


Figure 12. Pole figure showing the predicted inclination of CBBs in the crystallographic coordinate system, [100]-[010]-[001] for Type 2 grains whose [001] axis is inclined less than 6° from the tensile axis. $\epsilon_{VM} = 0.1$.

3.4.3. Type 3 grains

In grains oriented near the [111] pole, termed Type 3 grains, Huang, Winther and co-workers [11, 13, 15, 19–21] have observed non-crystallographic CBBs deviating 10° – 35° from the nearest $\{111\}$ plane. The nearest $\{111\}$ plane was identified as the cross-slip plane by Winther et al [15]. Further, Huang and Winther [19] have reported observing CBBs aligned with $\{115\}$ planes in grains closest to the [111] pole. In grains oriented further away from the [111] pole in the stereographic triangle, they have reported observing CBB segments within 10° of $\{35\bar{1}\}$ -type planes.

In agreement with the experimental observations, the present calculations predict misalignment in excess of 15° between the predicted CBBs and any of the $\{111\}$ planes, as seen from Figures 5 (a) and (b). The calculated part of the orientation space that corresponds to Type 3 grains is also shown in Figure 11. Also in agreement with experimental observations, CBB 2 in grains oriented near the [111] pole are most closely aligned with the cross slip plane, as seen from Figure 5 (d). It can also be seen from the same figure that some orientations located near [111] also show closest alignment of their CBB 2s with the critical slip plane. It thus appears that the single CBBs that form in Type 3 grains experimentally corresponds to CBB 2s in the present calculations even though, the $\dot{\rho}_{GND}b/\dot{\epsilon}_{VM}$ of CBB 2s is larger than that of the corresponding CBB 1s, as shown in Figure 8.

In Type 3 grains oriented near the [001]-[111] line the predicted CBBs align along (110) and $(\bar{1}10)$. This prediction diverges from the experimentally measured crystallographic planes ($\{35\bar{1}\}$ and $\{115\}$). Cahn [54] noted that rotation with the grain shape of CBBs formed along $\{110\}$ planes about a $\langle 112 \rangle$ direction lying in the $\{111\}$ slip plane will result in their coincidence with a $\{35\bar{1}\}$ plane after about 30% tensile strain. Together with the experimental observations, this suggests that CBB segments in Type 3 grains may be getting pinned at points along their length [24],

so that their orientation evolves following the grain shape. CBB pinning along the lines of intersection of two sets of CBBs has been observed by Wrobel et al. [55] in rolling deformation.

Another reason for the difference in the orientation of the predicted and observed CBBs, as noted at the beginning of Section 3.4, may be that the experimental observations pertain to the alignment of CBB segments with crystallographic planes, whereas the present calculations predict the gross orientation of CBBs relative to the average lattice orientation. The divergence of the predicted and measured crystallographic planes aligned with the CBBs suggests that the local crystallographic orientation of CBB segments that form the wavy and irregular Type 3 CBBs [11, 13, 15, 19] deviates substantially from the gross orientation of CBBs, unlike in Type 1 grains.

4. Conclusion

A general method to identify CBB disorientation and orientation in an arbitrarily oriented rigid-plastic rate-independent grain, which accommodates arbitrary imposed deformation by slip and whose slip systems are in an arbitrary but uniform state of hardness, is given on the basis of three physical hypotheses. The optimal CBB disorientation and orientation are obtained as those which minimize the plastic power of the grain and the incompatibility of plastic deformation across the CBB. Despite the uncertainties in the constraint experienced by individual grains, the predicted CBB orientations agree reasonably well with experimental observations in f.c.c. polycrystals subjected to uniaxial tensile deformation; the predicted subdivision of the orientation space into Types 1, 2 and 3 is comparable with the experimentally observed subdivision. This suggests that the assumed hypotheses may represent the physical principles underlying CBB orientation and disorientation preferences.

Acknowledgment: The author acknowledges valuable discussions with M. Arul Kumar and Ishan Sharma of IIT Kanpur. The author also acknowledges using Dr. C. N. Tomé's POLE software for plotting all the pole figures presented here. Funding was provided by the Indira Gandhi Centre for Atomic Research, Kalpakkam.

References

- [1] C. Tomé, G.R. Canova, U.F. Kocks, N. Christodoulou and J.J. Jonas, *Acta metall.* 32 (1984) p.1637–1653.
- [2] G.C. Butler and D.L. McDowell, *Int. J. Plast.* 14 (1998) p.703–717.
- [3] B. Peeters, M. Seefeldt, C. Teodosiu, S.R. Kalidindi, P.V. Houtte and E. Aernoudt, *Acta mater.* 49 (2001) p.1607–1619.
- [4] B. Peeters, B. Bacroix, C. Teodosiu, P.V. Houtte and E. Aernoudt, *Acta mater.* 49 (2001) p.1621–1632.
- [5] S. Mahesh, C.N. Tomé, R.J. McCabe, G.C. Kaschner, I.J. Beyerlein and A. Misra, *Metall Mater Trans A* 35 (2004) p.3763–3774.
- [6] B. Bay, N. Hansen and D. Kuhlmann-Wilsdorf, *Mater. Sci. Eng. A* 113 (1989) p.385–397.
- [7] M.F. Ashby, *Phil. Mag.* 21 (1970) p.399.
- [8] M. Seefeldt and P. Klimanek, *Modelling Simul. Mater. Sci. Eng.* 6 (1998) p.349–360.
- [9] R.D. McGinty and D.L. McDowell, *ASME J. Eng. Mater. Tech.* 121 (1999) p.203–209.
- [10] H. Christoffersen and T. Leffers, *Scripta mater.* 37 (1997) p.2041–2046.
- [11] X. Huang and N. Hansen, *Scripta mater.* 37 (1997).
- [12] G. Winther, D.J. Jensen and N. Hansen, *Acta mater.* 45 (1997) p.5059–5068.
- [13] X. Huang, *Scripta mater.* 38 (1998) p.1697–1703.
- [14] Q. Liu, D.J. Jensen and N. Hansen, *Acta mater.* 46 (1998) p.5819–5838.
- [15] G. Winther, X. Huang and N. Hansen, *Acta mater.* 48 (2000) p.2187–2198.
- [16] G. Winther, *Acta mater.* 51 (2003) p.417–429.
- [17] P.J. Hurley, P.S. Bate and F.J. Humphreys, *Acta mater.* 51 (2003) p.4737–4750.
- [18] X. Huang and N. Hansen, *Mater. Sci. Eng. A* 387–389 (2004) p.186–190.

- [19] X. Huang and G. Winther, *Phil. mag.* 87 (2007) p.5189–5214.
- [20] G. Winther and X. Huang, *Phil. mag.* 87 (2007) p.5215–5235.
- [21] G. Winther, *Acta mater* 56 (2008) p.1919–1932.
- [22] J.A. Wert and X. Huang, *Phil. Mag.* 83 (2003) p.969–983.
- [23] H. Christoffersen and T. Leffers, *Acta mater.* 46 (1998) p.4093–4102.
- [24] A. Albou, J.H. Driver and C. Maurice, *Acta mater* 58 (2010) p.3022–3034.
- [25] U.F. Kocks, C.N. Tomé and H.R. Wenk *Texture and Anisotropy*, Cambridge University Press, Cambridge, U.K., 1998.
- [26] G.I. Taylor, *J. Inst. Met.* 62 (1938) p.307.
- [27] J.F.W. Bishop and R. Hill, *Phil. Mag.* 42 (1951) p.414–427.
- [28] G.Y. Chin and W.L. Mammel, *Trans. AIME* 245 (1969) p.1211.
- [29] S. Mahesh, *Acta mater.* 54 (2006) p.4565–4574.
- [30] T. Leffers, *Int. J. Plast.* 17 (2001) p.469–489.
- [31] D.A. Hughes, D.C. Chrzan, Q. Liu and N. Hansen, *Phy. rev. letters* 81 (1998) p.4664–4667.
- [32] G.B. Dantzig *Linear programming and extensions*, Princeton University Press, Princeton, New Jersey, 1963.
- [33] W. Karush, *Minima of Functions of Several Variables with Inequalities as Side Constraints*; Master’s thesis, Univ. of Chicago (1939), .
- [34] Y.C. Chang, *N dimension golden section search: its variants and limitations*, in *Proc. 2nd Int. Conf. Biomedical Engineering and Informatics*, R. Shi, W. Fu, Y. Wang and H. Wang, eds., , 2009, p. 5304779.
- [35] R.A. Horn and C.R. Johnson *Matrix Analysis*, Cambridge University Press, Cambridge, 1985.
- [36] J. Lubliner *Plasticity theory*, MacMillan, 1998.
- [37] D. Kuhlmann-Wilsdorf, *Phil. Mag. A.* 79 (1999) p.955–1008.
- [38] M.A. Meyers and E. Ashworth, *Phil. Mag. A* 46 (1982) p.737–759.
- [39] G.Y. Chin and B.C. Wonsiewicz, *Trans. AIME* 245 (1969) p.871–872.
- [40] C.S. Lee, B.J. Duggan and R.E. Smallman, *Acta metall. mater.* 41 (1993) p.2265–2270.
- [41] M. Ortiz and E.A. Repetto, *J. Mech. Phys. Solids* 47 (1999) p.397–462.
- [42] M. Ortiz, E.A. Repetto and L. Stainier, *J. Mech. Phys. Solids* 48 (2000) p.2077–2114.
- [43] C. Carstensen, K. Hackl and A. Mielke, *Proc. R. Soc. Lond. A.* 458 (2002) p.299–317.
- [44] D.M. Kochmann and K. Hackl, *Continuum Mech. Thermodyn.* 23 (2011) p.63–85.
- [45] T. Leffers, *A model for rolling deformation with the grains subdivided into cell blocks*, , in *Proc. of the 13th Riso International Symposium on Mater. Sci.: Modeling of plastic deformation and its engineering applications*, 1992, p. 7.
- [46] S. Aubry and M. Ortiz, *Proc. R. Soc. Lond A* 459 (2003) p.3131–3158.
- [47] S.M. Sivakumar and M. Ortiz, *Comput. Methods Appl. Mech. Engrg.* 193 (2004) p.5177–5194.
- [48] N.A. Fleck, M.F. Ashby and J.W. Hutchinson, *Scripta mater.* 48 (2003) p.179–183.
- [49] J.F. Nye, *Acta metall.* 1 (1953) p.153.
- [50] S. Sun, B.L. Adams and W.E. King, *Phil. mag.* 80 (2000) p.9–25.
- [51] R. Abbaschian, L. Abbaschian and R.E. Reed-Hill *Physical Metallurgy Principles*, Cengage, 2008.
- [52] R.J. McCabe, A. Misra and T.E. Mitchell, *Acta mater.* 52 (2004) p.705–714.
- [53] H.F. Poulsen, L. Margulies, S. Schmidt and G. Winther, *Acta mater.* 51 (2003) p.3281–3830.
- [54] R.W. Cahn, *J. Inst. Metals* 79 (1951) p.129–158.
- [55] M. Wrobel, S. Dymek, M. Blicharski and S. Gorczyca, *Z. Metallkunde* 85 (1994) p.415–425.
- [56] S. Mahesh, *Int. J. Plast.* 25 (2009) p.752–767.
- [57] M. Arul Kumar, S. Mahesh and V. Parameswaran, *Int. J. Plasticity* 27 (2011) p.962–987.

Appendix A. The lower bound theorem

Let $\boldsymbol{\sigma}^*(\boldsymbol{x})$ be a “trial” deviatoric stress field in a rigid-plastic body which, (i) satisfies the equilibrium equations everywhere and (ii) does not violate the yield criterion anywhere. The strain-rates associated with the trial field, $\boldsymbol{\sigma}^*(\boldsymbol{x})$, need not be compatible. Let $\boldsymbol{\sigma}(\boldsymbol{x})$ denote the true deviatoric stress field in the body, i.e., which in addition to (i) and (ii) above, also satisfies the compatibility conditions everywhere. Let the true compatible strain-rate field in the body be $\dot{\boldsymbol{\epsilon}}(\boldsymbol{x})$. The principle of maximum plastic power [36] maintains that the plastic power of the trial field, $\boldsymbol{\sigma}^*(\boldsymbol{x})$, can be no greater than that of the true field, $\boldsymbol{\sigma}(\boldsymbol{x})$, i.e.,

$$\int \boldsymbol{\sigma}(\boldsymbol{x}) : \dot{\boldsymbol{\epsilon}}(\boldsymbol{x}) \, d\boldsymbol{x} \geq \int \boldsymbol{\sigma}^*(\boldsymbol{x}) : \dot{\boldsymbol{\epsilon}}(\boldsymbol{x}) \, d\boldsymbol{x}, \quad (\text{A1})$$

where both integrals range over the volume of the body.

Consider a collection of standard rate-independent material points of volume fractions $\rho^{(1)}, \rho^{(2)}, \dots$ such that $\sum_i \rho^{(i)} = 1$. Each material point is assumed to deform homogeneously. The s -th Schmid tensor associated with the i -th material

point will be denoted $\mathbf{m}_s^{(i)}$. In general, $\mathbf{m}_s^{(i)} \neq \mathbf{m}_s^{(j)}$ for distinct material points i and j , $i \neq j$.

The material points are said to collectively accommodate the imposed velocity gradient $\bar{\mathbf{L}}$ if

$$\bar{\mathbf{L}} = \sum_i \rho^{(i)} \mathbf{L}^{(i)}, \tag{A2}$$

where $\mathbf{L}^{(i)}$ denotes the velocity gradient of the i -th material point. Taking only the symmetric part of both sides in Equation (A2),

$$\bar{\boldsymbol{\epsilon}} = \sum_i \rho^{(i)} \dot{\boldsymbol{\epsilon}}^{(i)}, \tag{A3}$$

where, $\dot{\boldsymbol{\epsilon}}^{(i)}$ denotes the strain-rate of the i -th material point and $\bar{\boldsymbol{\epsilon}} = (\bar{\mathbf{L}} + \bar{\mathbf{L}}^T)/2$ denotes the imposed strain rate. Together with a consistent set of compatibility conditions, Equation (A3) determines the state of stress, $\boldsymbol{\sigma}^{(i)}$, in each material point i [56, 57].

The principle of maximum plastic power is now applied to the collection of discrete material points. The integrals in Equation (A1) now reduce to summations. For any set of trial deviatoric stresses $\boldsymbol{\sigma}^{*(1)}, \boldsymbol{\sigma}^{*(2)}, \dots$, at the material points, which are in equilibrium and do not violate the yield condition (i.e., satisfy $\boldsymbol{\sigma}^{*(i)} : \mathbf{m}_s^{(i)} \leq 0$, for all i , and s), Equation (A1) becomes

$$\sum_i \rho^{(i)} \boldsymbol{\sigma}^{(i)} : \dot{\boldsymbol{\epsilon}}^{(i)} \geq \sum_i \rho^{(i)} \boldsymbol{\sigma}^{*(i)} : \dot{\boldsymbol{\epsilon}}^{(i)}. \tag{A4}$$

If the trial stress field is further required to be uniform, i.e.,

$$\boldsymbol{\sigma}^{*(1)} = \boldsymbol{\sigma}^{*(2)} = \dots = \bar{\boldsymbol{\sigma}}^*, \tag{A5}$$

where, $\bar{\boldsymbol{\sigma}}^*$ denotes the uniform stress over all the material points, equilibrium follows trivially [25] and the yield condition takes the form

$$\bar{\boldsymbol{\sigma}}^* : \mathbf{m}_s^{(i)} \leq \tau_s, \quad \forall i, s. \tag{A6}$$

Equation (A4) becomes

$$\begin{aligned} \sum_i \rho^{(i)} \boldsymbol{\sigma}^{(i)} : \dot{\boldsymbol{\epsilon}}^{(i)} &\geq \sum_i \rho^{(i)} \bar{\boldsymbol{\sigma}}^* : \dot{\boldsymbol{\epsilon}}^{(i)}, \\ &= \bar{\boldsymbol{\sigma}}^* : \sum_i \rho^{(i)} \dot{\boldsymbol{\epsilon}}^{(i)}, \\ &= \bar{\boldsymbol{\sigma}}^* : \bar{\boldsymbol{\epsilon}}, \end{aligned} \tag{A7}$$

where, Equation (A3) has been used in the last step. It has thus been shown that

$$P_{\min} = \bar{\boldsymbol{\sigma}}^* : \bar{\boldsymbol{\epsilon}} \leq \sum_i \rho^{(i)} \boldsymbol{\sigma}^{(i)} : \dot{\boldsymbol{\epsilon}}^{(i)} \equiv P, \tag{A8}$$

where, $\bar{\boldsymbol{\sigma}}^*$ satisfies Equation (A6) and $\dot{\boldsymbol{\epsilon}}^{(i)}$ obey Equation (A3). This result is used in the sequel, with the identification of material points with cell blocks.